

Lightwave-driven electrons in a Floquet topological insulator

Tobias Weitz,^{1,*} Daniel M. B. Lesko,^{1,*} Simon Wittigschlager,¹
Weizhe Li,¹ Christian Heide,^{1,2} Ofer Neufeld,³ and Peter Hommelhoff¹

¹*Department of Physics, Friedrich-Alexander-Universität Erlangen-Nürnberg (FAU), Erlangen, Germany*

²*Stanford PULSE Institute, SLAC National Accelerator Laboratory, Menlo Park, CA, USA*

³*Max Planck Institute for the Structure and Dynamics of Matter, Hamburg, Germany*

(Dated: July 26, 2024)

Topological insulators offer unique opportunities for novel electronics and quantum phenomena [1, 2]. However, intrinsic material limitations often restrict their applications and practical implementation. Over a decade ago it was predicted that a time-periodic perturbation can generate out-of-equilibrium states known as Floquet topological insulators (FTIs) [3–6], hosting topologically protected transport and anomalous Hall physics, and opening routes to optically-tunable bandstructures and devices compatible with petahertz electronics. Although such states have not yet been directly observed, indirect signatures such as the light-induced anomalous Hall effect were recently measured [7]. Thus far, much remained experimentally unclear and fundamentally unknown about solid-state FTI and whether they can be employed for electronics. Here we demonstrate coherent control of photocurrents in light-dressed graphene. Circularly-polarized laser pulses dress the graphene band structure to obtain an FTI, and phase-locked second harmonic pulses drive electrons in the FTI. This approach allows us to measure resulting all-optical anomalous Hall photocurrents, FTI-valley-polarized currents, and photocurrent circular dichroism, all phenomena that put FTIs on equal footing with equilibrium topological insulators. We further present an intuitive description for the sub-optical-cycle light-matter interaction, revealing dynamical symmetry selection rules for photocurrents. All measurements are supported by strong agreement with *ab-initio* and analytic theory. Remarkably, the photocurrents show a strong sub-cycle phase-sensitivity that can be employed for ultrafast control in topotronics and spectroscopy. Our work connects Floquet and topological physics with attoscience and valleytronics, and goes beyond band structure engineering by initiating lightwave-driven dynamics in FTI states.

While first predicted in solids [3, 4], Floquet topological physics has been experimentally studied in optical lattices and photonics primarily, where effects of interactions and decoherence can usually be ignored [8–13].

Only recently, McIver et al. experimentally measured anomalous Hall currents in light-dressed graphene [7], where the system enters an out-of-equilibrium Floquet topological insulator (FTI) steady-state driven by circularly-polarized light.

FTIs exhibit topological and quantum properties dramatically different from the equilibrium (field-free) states. Lifted from the material constraints of intrinsic topological insulators, solid state FTIs offer high tunability with the driving laser field properties and the choice of the underlying material system. Intriguingly, Floquet dressing can be used for synthesizing almost arbitrary material band structures with varying topological phases, inducing gap openings, and enabling control over valley pseudospin degrees of freedom and anomalous Hall phenomena [7, 14]. Despite this progress, Floquet topological states have not yet been directly observed, and only recently Floquet bands in graphene were reported in the topologically trivial state [15, 16] following earlier observations in other materials [17, 18]. Understanding how to control and utilize FTIs for topologically-protected electronics such as photocurrent generation remains an important milestone both fundamentally and toward applications.

In parallel to dressed band structure developments, strong-field phenomena in solids have shown the route to probe sub-optical cycle and attosecond electron dynamics in out-of-equilibrium systems [19–22], including in topological insulators [23–28], and valley physics in hexagonal solids [29, 30]. However, ultrafast dynamics in FTIs have not yet been explored. An ideal approach would be to merge the attosecond lightwave picture, which is fully-optical, with the concept of Floquet physics based on transport measurements that are a cornerstone in condensed matter physics (in this case without DC or magnetic fields), potentially enabling control with simultaneous analysis of topological and sub-optical-cycle attosecond phenomena. Here we accomplish this and pave the way to Floquet topotronics and its lightwave implementation.

CIRCULAR DICHRISM AND ALL-OPTICAL ANOMALOUS HALL EFFECT IN AN FTI

We optically dress bare graphene (Fig. 1a) by irradiation with a circularly-polarized fundamental (ω) laser field (Fig. 1b). This 'dressing' field generates

* These authors contributed equally to this work.

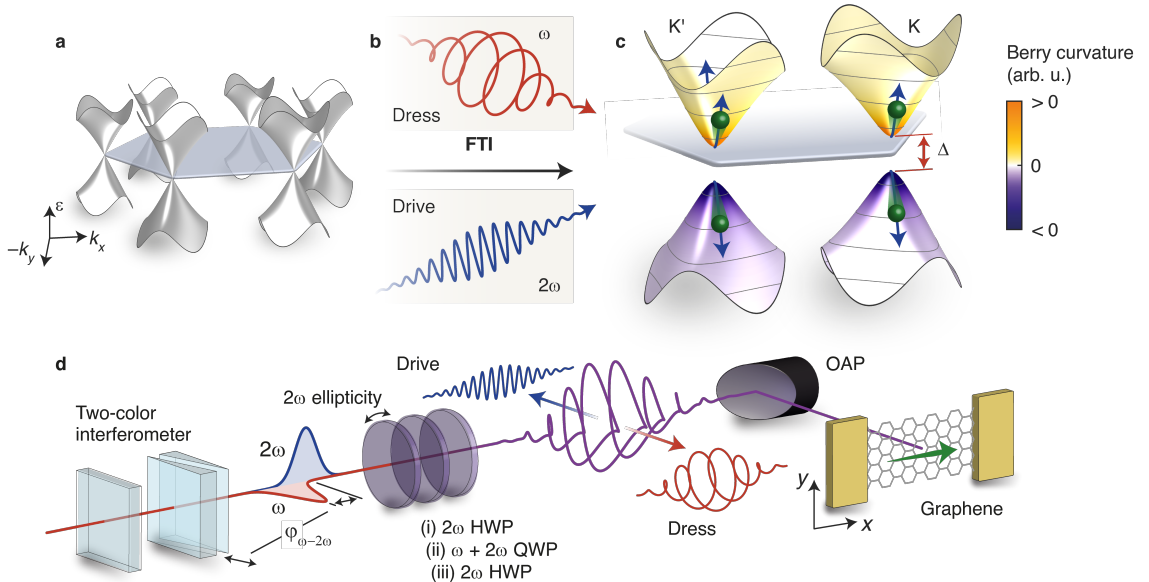


FIG. 1. **Lightwave control of electrons in a Floquet topological insulator.** **a–c**, A Floquet topological insulator (FTI) emerges from driving the gapless, topologically trivial band structure of graphene (**a**) by irradiating it with a circularly-polarized fundamental laser field (**b**, red waveform). This dressing breaks inversion and time-reversal symmetry, giving rise to both a nonzero gap Δ at the emerging K and K' valleys and a Berry curvature of the same sign, resulting in a non-zero Chern number and a non-trivial topological insulating phase (**c**). A second harmonic pulse (**b**, blue waveform) controls the motion of electrons in the FTI bands. By changing the ellipticity of the 2ω pulse we probe the topology of the FTI by measuring circular dichroism and the anomalous Hall effect via photocurrents. **d**, Sketch of the experimental setup. The $\varphi_{\omega-2\omega}$ between the co-propagating ω and 2ω pulses is controlled in a collinear two-color interferometer. In a sequence of dichroic half-waveplates (HWP) and a superachromatic quarter-waveplate (QWP; see Methods) we shape the ω circular dress and the 2ω drive pulse with arbitrary polarization. Using an off-axis parabolic mirror (OAP), we focus the resulting waveform on a monolayer graphene strip, mounted in a vacuum chamber (not shown). We measure $\varphi_{\omega-2\omega}$ - and polarization-dependent photocurrents via gold electrodes attached to the graphene strip.

gapped Floquet-Bloch bands with broken time reversal symmetry, forming a topologically non-trivial state (Fig. 1c) [3, 4]. In this transient FTI bandstructure, a second 'drive' laser pulse with carrier frequency (2ω) drives coherent ultrafast electron dynamics in the dressed state, generating photocurrents. The dressed band picture is well-justified by the topological indices and laser parameters of the system [31–33] (see Methods for details), and should naturally give rise to the anomalous Hall effect and dichroic responses. Moreover, since both fields share the same fundamental periodicity for any laser parameters, the Floquet approach remains valid throughout. For these reasons, we adopt it for the main analysis of the physical mechanisms, though below we will also present a different picture where both optical fields can be thought of as driving photocurrent responses simultaneously. By varying the relative phase $\varphi_{\omega-2\omega}$ between the fields (Fig. 1d) we can probe the FTI states' phases (the attosecond sub-optical-cycle micromotion [34, 35]). Furthermore, by changing the drive pulse ellipticity we probe the FTI Hamiltonian's symmetry and symmetry breaking [11, 31]. Thus, this approach provides a route to directly visualize quantum phenomena arising from the transient light-dressed FTI state stroboscopically.

We experimentally measure optical waveform-dependent photocurrents resulting from the two-color set-up for different ellipticities and relative phases. The optical setup used for the synthesis of the two fields is sketched in Fig. 1d. Part of the light from an 80 MHz erbium fiber laser is frequency doubled to form 2ω pulses with a photon energy of 1.6 eV (775 nm, 110 fs intensity full width at half maximum, FWHM), which we overlap in a highly stable collinear setup with the fundamental ω pulses at 0.8 eV (1550 nm, 170 fs FWHM). The relative phase $\varphi_{\omega-2\omega}$ between the pulses is controlled by calcite wedges in the collinear two-color interferometer [36]. After polarization control with a sequence of dichroic waveplates, the pulses are focused onto epitaxial monolayer graphene on silicon carbide using an off-axis parabolic mirror. The resulting currents are measured via attached gold electrodes. The fundamental field strength at the sample focus is measured to be 0.27 V nm^{-1} , with a 3:4 field ratio of second harmonic to fundamental (equivalently, a ratio of 3:8 in vector potential, see Methods for details).

As our Floquet topological insulating state is generated by the circularly-polarized ω field, we can probe topological phenomena such as circular dichroism [17, 37, 38] and the anomalous Hall effect [3, 10, 14] by tuning the drive 2ω field polarization (Fig. 2). This takes full advantage

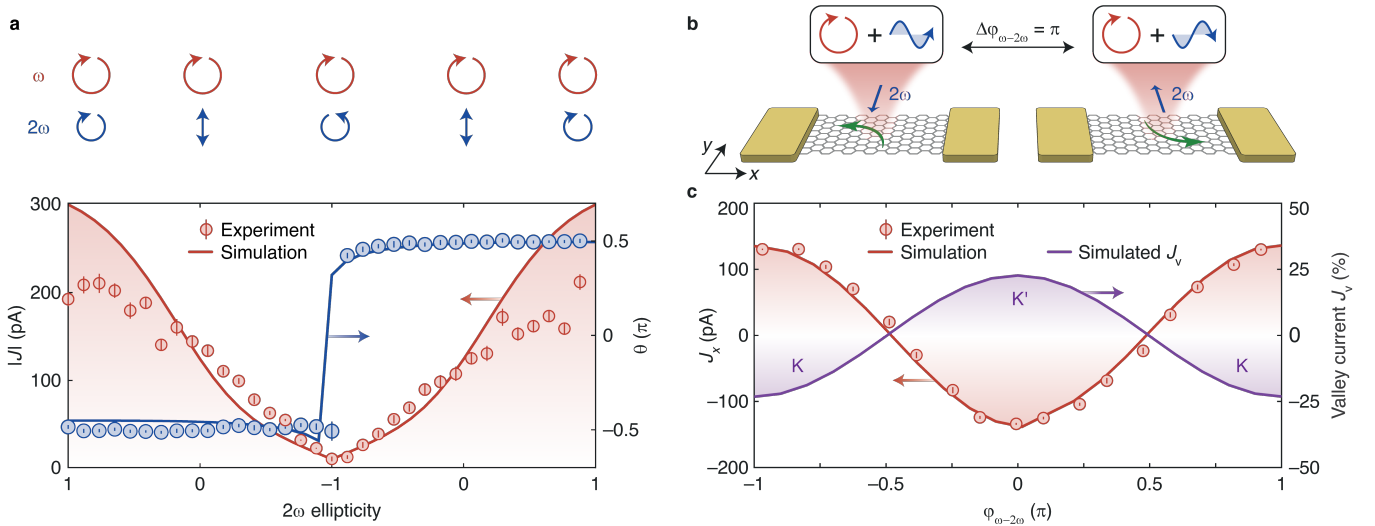


FIG. 2. **Signatures of the topologically insulating phase in photocurrent measurements.** **a**, We probe circular dichroism by keeping the helicity of ω constant, generating the FTI, and continuously sweep the ellipticity of 2ω (above). Below, measured current amplitude $|J|$ (red circles) and phase θ (blue circles) as a function of the 2ω ellipticity. TDDFT simulation results (red line) support the dichroic generation of ballistic photocurrent for co-rotating helicities of ω and 2ω and suppression for counter-rotating helicities. **b**, Anomalous lightwave-driven Hall currents (green arrows) emerge from excitation of the ω -driven FTI with 2ω control polarized perpendicularly to the electrode axis. Flipping $\varphi_{\omega-2\omega}$ by π effectively results in a reversal of the 2ω deflection and consequently also the Hall current direction. **c**, Measured current (red circles) as a function of $\varphi_{\omega-2\omega}$. The computed current density (red line) confirms the directional control of the anomalous Hall effect. The computed degree of valley polarized current J_v (purple line) reaches nearly 25% realizing preferential current generation from either K or K'. For the *ab-initio* calculations, pulses at 1550 nm with $E_0 = 0.27 \text{ V nm}^{-1}$ are employed with 75% 2ω field admixture. Error bars indicate ten times the standard deviation.

of the Floquet Hamiltonian's periodicity by employing both polarization- and $\varphi_{\omega-2\omega}$ -dependent measurements.

We first analyze the circular dichroism by measuring the 2ω ellipticity-dependent photocurrent at $\varphi_{\omega-2\omega} = 0$ (Fig. 2a). Common to angle-resolved photoemission spectra [37], the Berry curvature $\Omega(\mathbf{k})$ of the topological insulator dictates which optical probe pulse helicity can generate photocurrents (momentum imbalance of populations). When the helicity of the second harmonic matches/anti-matches the sign of the Berry curvature of the FTI, we obtain a strong asymmetric/symmetric population, resulting in a photocurrent enhancement/suppression. We observe this experimentally as a suppression of the photocurrent by nearly two orders of magnitude as the 2ω helicity goes from $\epsilon = 1$ to $\epsilon = -1$, while the ω helicity is fixed to $\epsilon = 1$, preserving the sign of Ω (Fig. 1c). These results are well matched by *ab-initio* time-dependent density functional theory simulations (TDDFT, full line in Fig. 2a, see Methods). We stress that the circular dichroism is obtained by reversing the helicity of the drive, and not that of the dressing field, while undressed graphene has no circular dichroic response due to its inversion symmetry. Hence, this represents a fundamental measure of the FTI state's intrinsic non-trivial dichroic response, enabled by the optical approach we employ.

Next, we investigate the ultrafast motion of electrons driven by a linearly polarized drive pulse with a circularly-polarized dressing pulse. Due to the curl of

the Berry curvature of the FTI and intraband motion, $\dot{\mathbf{k}}(t) = -(e/\hbar)\mathbf{E}_{2\omega}$ ($e > 0$, elementary charge; \hbar , reduced Planck's constant), the second harmonic field $\mathbf{E}_{2\omega}$ may produce a current density from excited populations ρ^c in the orthogonal direction, $\mathbf{j} = -\rho^c(e/\hbar)\mathbf{E}_{2\omega} \times \Omega$, known as the anomalous Hall effect [3, 7, 14] (schematically shown in Fig. 2b, with \mathbf{k} the electron wave vector, e the electron charge, and \hbar the reduced Planck constant). Here, we orient the linear polarization of the second harmonic in y -direction, orthogonal to the measurement electrodes, and measure $\varphi_{\omega-2\omega}$ -dependent currents (Fig. 2c). We expect that as the relative phase is varied, the anomalous Hall current will reverse. This is equivalent to an effective reversal of a 'DC' bias voltage, similar to that measured in [7], and is all-optically sensing the sub-cycle phase of the FTI states [11, 34]. In a complete mapping of the photocurrent as a function of the two color phase (Fig. 2c), we observe a reversal of the current between $\varphi_{\omega-2\omega} = 0$ and π , showing that the optical phase controls the anomalous Hall current direction. Our measurements represent the first all-optical anomalous Hall effect in dressed graphene, coherently controlled by attosecond sub-cycle optical delays.

Ab-initio TDDFT simulations (Fig. 2a, c) agree remarkably well with the experiment (see Methods for details), implying that we can rule out the contribution of edge states in this geometry. Further analysis of TDDFT results suggests that the primary mechanism is from Floquet physics, due to both the dominate role of the first

valence and conduction bands of graphene, and the lack of observed electron-electron interactions (see Methods).

The excellent agreement of experiment and theory allows us to unravel the origin of the currents: A decomposition of the current into its contributions from the K and K' valley shows that it is 25% valley selective (Fig. 2c purple line), i.e. one valley carries a larger population imbalance (see Methods). This strikingly means that the FTI valleys around K and K' can be used for valleytronics, establishing FTI-based valleytronics.

LIGHTWAVE-DRIVEN PHOTOCURRENTS IN GRAPHENE

FTI bands are strictly time periodic due to the Floquet formalism [5, 6], which precludes straightforward analysis of the sub-cycle electron dynamics. To understand how these dynamics and waveform symmetries dictate photocurrent generation, we explore the complimentary composite waveform picture (of both ω and 2ω) driving electron motion in the *undressed* graphene bands. We focus on the interaction with three specific waveforms with Lissajous figures shown in Figs. 3a-c. These Lissajous result from the superposition of the fundamental laser fields (ω) and its second harmonic (2ω) with properly chosen polarization states and $\varphi_{\omega-2\omega}$ (Fig. 1c). To understand the emergence of photocurrents and valley polarization from the qualitatively different momentum fingerprints (Figs. 3d-f), we will first compare the respective electron intraband trajectories $\mathbf{k}(t)$ in bare graphene, the optical waveform symmetries, and the associated interband excitations. These aspects will complement and expand the FTI-based discussion results.

With opposite helicities of fundamental and second harmonic, a counter-rotating circularly-polarized (CNR) waveform emerges and exhibits a three-fold rotational dynamical symmetry (Fig. 3b) [39]. Upon tuning $\varphi_{\omega-2\omega}$, its Lissajous can be oriented such that it matches the trigonal warping at K' and anti-matches it at the K valley, or vice versa. Accordingly, electrons driven in the two valleys may experience a different excitation probability, yielding an inter-valley occupation imbalance, i.e., *valley polarization* (Fig. 3e, red vs. blue shading) [29, 30, 40, 41]. This can be understood with the broken time-reversal symmetry of the Lissajous figures. The population has rotational symmetry around each valley, such that no ballistic current is excited. The two other cases shown in Fig. 3 are discussed in detail in the Methods, where we overall see that the co-rotating (COR) waveform leads to roughly equal ballistic currents from both valleys, whereas the TD waveform leads to a current dominantly arising from one valley only, i.e., a *valley current*.

To experimentally investigate these three distinct cases, we map out photocurrents as a function of all relevant 2ω polarization states and phases (Fig 4a). On the vertical axis, as we tune the 2ω ellipticity while keep-

ing ω circular, we continuously sweep from a COR to a TD and a CNR waveform and further to a TD and COR waveform again. As the fast and slow axes of the 2ω half waveplate are interchanged by sweeping across ellipticity -1 , a π phase jump is introduced between the two colors, resulting in an inversion of current direction with approximately identical amplitudes for equal ellipticities > -1 . The remarkably large magnitude of up to 214 pA obtained for the COR waveform can be assigned to the substantially more efficient momentum symmetry breaking compared to CEP-controlled current generation [42-45]. As the waveplate is rotated to generate the TD waveform, $|J|$ decreases to approximately 140 pA. Finally, with the CNR waveform, $|J|$ further decreases to a minimum of 12 pA. Importantly, the strong overall suppression of current injection supports the generation of valley polarization by the bichromatic waveforms (see Methods).

Changing $\varphi_{\omega-2\omega}$ with the two-color interferometer results in a continuous rotation of the Lissajous figures, which we observe experimentally as a sinusoidal oscillation of injected current (Fig. 4a and lineouts, solid circles, in Fig. 4b). This oscillatory behavior as function of $\varphi_{\omega-2\omega}$ is well known for $\omega - 2\omega$ coherent control [31, 46, 47], which we will connect below with dynamical symmetry selection rules imposed by the excitation waveform [39, 48]. Overlaid on the experimental data is the calculated current from TDDFT without any free parameters (normalized to the TD waveform current amplitude, see Methods). We observe similar sinusoidal behaviour between the experiment and theory, as well as a small non-zero current for the CNR waveform with a phase shifted maximum, showing remarkable agreement with the measurement.

SYMMETRIES, SELECTION RULES AND SUB-CYCLE DYNAMICS

For further insight, it is highly instructive to investigate how the $\omega - 2\omega$ light field symmetries are reflected in the excited state populations. This will also connect the sub-optical-cycle electron motion in the *undressed* band structure to the topological phenomena present in the FTI picture.

Figures 5a-d show the residual conduction band distributions for the CNR waveform obtained from TDDFT (see Methods). Analyzing all six K and K' points allows us to look at the dynamical selection rules for the respective waveforms globally, while the zoom-ins (Figs. 5c-d) highlight the intra-valley symmetries [39, 48]. Two symmetries dominate: (i) a mirror axis coupled to time-reversal arising in all field geometries (dashed green lines), and (ii) a three-fold rotational symmetry coupled to time translations arising in the CNR case only. These operators are symmetries of the full Floquet Hamiltonian in each specific case, and transfer onto the momentum distributions. Critically, from these symmetries we can

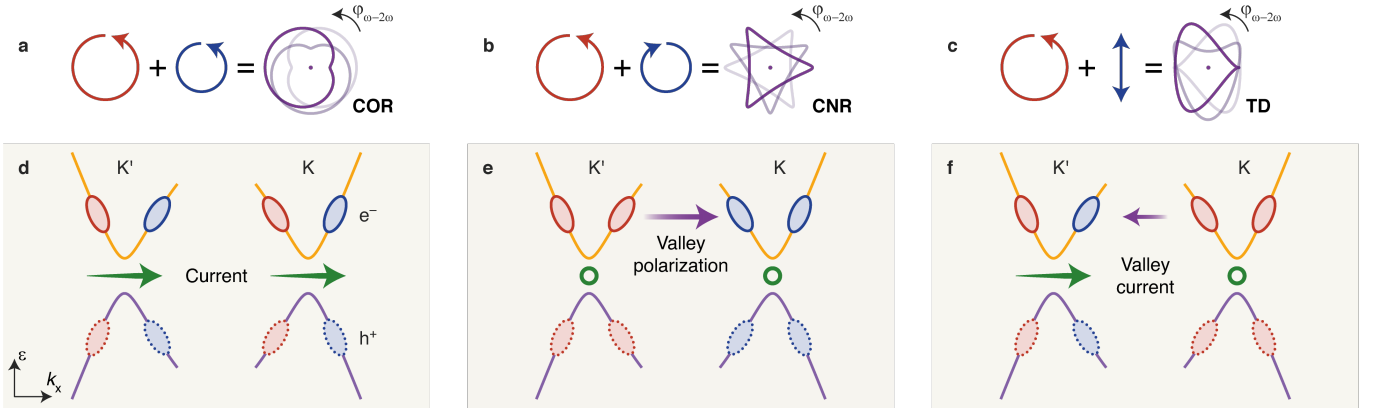


FIG. 3. Lightwave-driven valley excitation. We focus on three examples of the superposition of $\omega + 2\omega$ fields resulting in co-rotating circularly polarized (**a**, COR), counter-rotating circularly polarized (**b**, CNR), and teardrop polarized (**c**, TD) waveforms, with variable orientation determined by the two-color phase ($\varphi_{\omega-2\omega}$). **d-f**, Schematic carrier excitation achieved with a COR, a CNR, and a TD polarized waveform, resulting in currents from both valleys (**d**), valley polarization (**e**), and a valley-selective current, or for short valley current (**f**). The red (blue) features in (**d-f**) schematically indicate more (less) residual electron/hole excitation (full/dotted outline) after passage of the laser pulses. They result in a (valley) current (green arrows) or valley polarization (purple arrows) when a left-right asymmetry is generated either within at least one of the two valleys individually (intra-valley asymmetry like in (**d**) or in (**f**) around K') or between the two valleys (inter-valley like in (**e**)). We note that in the CNR case (**e**) no current can result because momentum symmetry is preserved within each valley. The TD case (**f**) can lead to both valley current and valley polarization. We can vary which valley (K and K') is addressed by continuously rotating the orientation via a change in the relative phase $\varphi_{\omega-2\omega}$.

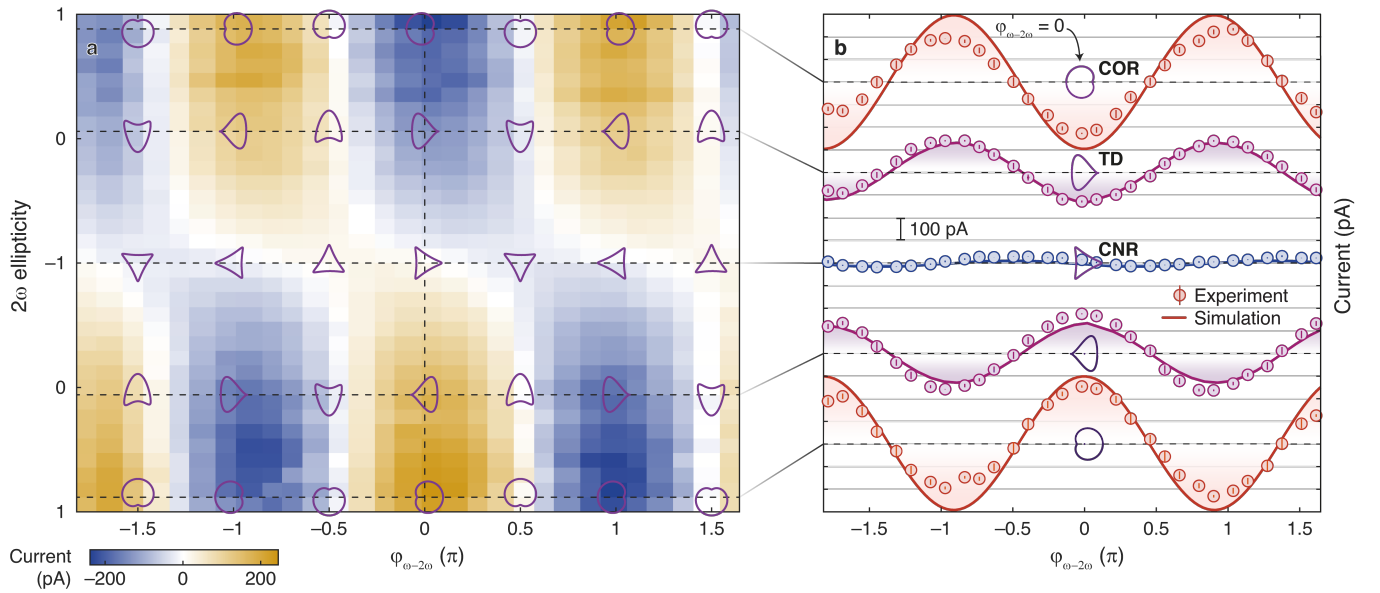


FIG. 4. Relative phase and polarization control over measured photocurrents. **a**, 2D map of relative phase-dependent current as a function of $\varphi_{\omega-2\omega}$ and the 2ω ellipticity. The insets exemplify the Lissajous figure transformation. **b**, Lineouts (horizontal dashed lines in (**a**)) as a function of $\varphi_{\omega-2\omega}$ indicating the generation of current (red, COR), valley current (purple, TD) and valley polarization (blue, CNR) in the absence of current. Circles represent experimental data with error bars of ten times the standard deviation, solid lines indicate results from TDDFT.

assign selection rules to how the light field symmetries dictate phenomena such as valley polarization, representing the first experimental mapping (Fig. 4a) of these dynamical symmetry selection rules.

We analyze the dynamical selection rules by the momentum distributions in tandem to points in the two-color parameter space where the residual measured cur-

rent is experimentally zero (i.e., indicating a forbidden injection current). For the CNR waveforms (Figs. 5a-b) we see one mirror axis present in the respective electron excitation distributions: For $\varphi_{\omega-2\omega} = \pi/2$ (Fig. 5a), we observe a symmetry axis through M- Γ -M (dashed green line), rendering ρ^c at K and K' symmetric. This symmetry hence results in the inability to generate a valley

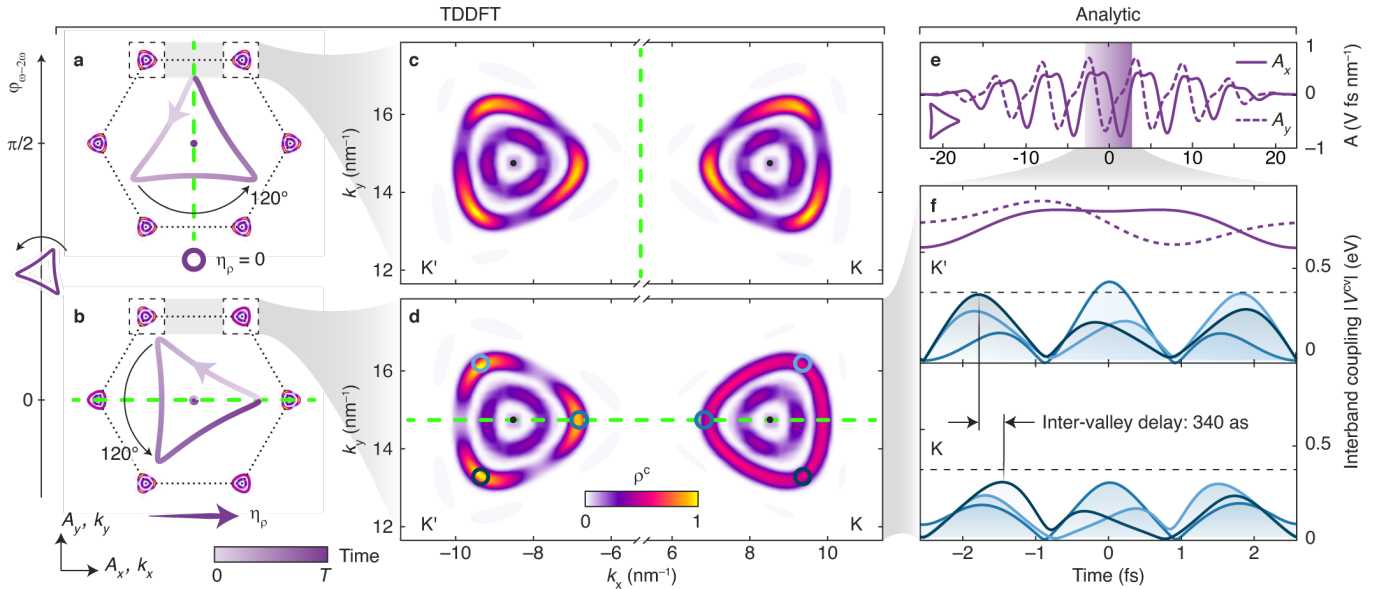


FIG. 5. **Sub-cycle dynamical symmetry selection rules.** **a–b**, Temporal shape and symmetries of the vector potential Lissajous figures (purple lines) and the resulting symmetries of residual momentum distributions ρ^c imprinted to the first Brillouin zone (dotted hexagons) for the CNR waveforms for $\varphi_{\omega-2\omega} = \pi/2$ and 0 respectively. The momentum distributions are computed with TDDFT (see Methods for details). Green dashed lines indicate global symmetry axes, determined by both waveform and time periodicity (see purple color bar). **c–d**, Close-ups of ρ^c around K and K' as indicated in **a**, **b**. For all cases, an eight-cycle pulse (vector potential in **e**) is applied with 1550nm fundamental wavelength with a peak field strength $E_0 = 0.27\text{V nm}^{-1}$ and 75% 2ω field admixture. **e**, CNR vector potential waveform for $\varphi_{\omega-2\omega} = 0$. The shaded area indicates the center optical cycle. **f**, temporal profile of the interband dipole coupling $|V^{cv}|$ [49] induced by the waveforms shown in **e**. The different shades of blue refer to initial momenta in the K and K' valley as marked with circles in panel **d**. The dashed black guide lines compare the $|V^{cv}|$ amplitudes at K and K' .

polarization. With $\varphi_{\omega-2\omega} = 0$, the waveform's symmetry axis ($K\text{-}\Gamma\text{-}K'$) now *disconnects* the K and K' points along k_x , allowing for the FTI valleys to be addressed differently. This results in a non-zero valley polarization of $\eta_\rho = 1\%$ (see Methods), which could be increased with more adiabatic driving parameters [40, 50]. The zoom-ins of the CNR population (Figs. 5c, d) reveal the local ρ^c symmetries within the K and K' valleys. The rotational dynamical symmetry in the CNR case in any case implies that the total injection current should vanish (since current from all K and K' points individually cancel each other). Experimentally (and numerically in TDDFT) we observe a very small residual current that arises from breaking of time-translational symmetry by the pulse envelope itself (i.e., departing from an infinitely time-periodic Floquet Hamiltonian). The COR waveform is further analyzed in the Methods section.

To understand the emergence of the characteristic ρ^c patterns in Fig. 5d on a sub-cycle time scale, it is insightful to further discuss the time-dependent inter- and intraband electron dynamics, in the *undressed* band structure. We highlight these dynamics for three exemplary electrons with initial momenta equidistant to the respective K and K' points (Fig. 5d, colored circles). Figure 5f shows the respective sub-cycle evolution of the interband dipole coupling $V^{cv}(t) = \mathbf{E}(t) \cdot \mathbf{d}^{cv}$ (instantaneous Rabi frequency modulo \hbar), which approximates the instan-

taneous excitation probability for a given electric field $\mathbf{E}(t)$ and an interband transition dipole matrix element $\mathbf{d}^{cv}(\mathbf{k}(t))$ [49]. The stark inter-valley differences in $|V^{cv}|$ occurring during the center optical cycle (Fig. 5e, shaded area) become clear with the corresponding trajectories drawn in Fig. 5f: Differences in the sub-femtosecond trajectories of electrons between K and K' show how the composite light field can be used to understand the valley selective physics (see Methods for more details). By looking at the coupling strength peaks, we observe inter-valley population differences forming within a time delay of 340 attoseconds between two k -space mirrored points, showing how time reversal, waveform, and band structure symmetries play a deep role in FTI physics.

CONCLUSION

We have demonstrated topological photocurrents from a Floquet topological insulator, measuring the all-optical anomalous Hall effect and photocurrent circular dichroism. The photocurrents show an exceedingly strong phase and ellipticity dependence, allowing us to use them to probe the ultrafast dynamics in the FTI. Strong agreement with *ab-initio* theory allowed us to pinpoint the source of currents to the FTI valleys at K and K' . For specific cases we considered the interaction of the two-

color light field with the bare material, revealing experimentally measured lightwave dynamical symmetry photocurrent selection rules. This symmetry picture maps the sub-optical-cycle electron motion onto the topological photocurrents, showing the deep connection between the lightwave symmetries and the FTI states.

Our work heralds Floquet topotronics, where topology is designed by an optical dressing field, unconstrained by material properties, and electrons are driven by a second field in the resulting FTI band structure, on (sub-) femtosecond time scales.

Most importantly, we experimentally demonstrated valley current generation (with a notable magnitude of 31 pA) from a Floquet topological insulator, realizing a decades long goal for valleytronics, and further showing that valleytronics can now be explored in inversion-symmetric materials that are not even required to exhibit valleys in their ground state. Furthermore, we foresee direct ramifications for novel material design, lightwave electronics, topological quantum computing, sensing, and ultrafast spectroscopy.

-
- [1] Hasan, M. Z. & Kane, C. L. Colloquium: Topological insulators. *Reviews of Modern Physics* **82**, 3045–3067 (2010).
- [2] Wieder, B. J. *et al.* Topological materials discovery from crystal symmetry. *Nature Reviews Materials* **7**, 196–216 (2021).
- [3] Oka, T. & Aoki, H. Photovoltaic Hall effect in graphene. *Physical Review B* **79**, 081406(R) (2009).
- [4] Lindner, N. H., Refael, G. & Galitski, V. Floquet topological insulator in semiconductor quantum wells. *Nature Physics* **7**, 490–495 (2011).
- [5] Oka, T. & Kitamura, S. Floquet engineering of quantum materials. *Annual Review of Condensed Matter Physics* **10**, 387–408 (2019).
- [6] Rudner, M. S. & Lindner, N. H. Band structure engineering and non-equilibrium dynamics in Floquet topological insulators. *Nature Reviews Physics* **2**, 229–244 (2020).
- [7] McIver, J. W. *et al.* Light-induced anomalous Hall effect in graphene. *Nature Physics* **16**, 38–41 (2019).
- [8] Rechtsman, M. C. *et al.* Photonic Floquet topological insulators. *Nature* **496**, 196–200 (2013).
- [9] Aidelsburger, M. *et al.* Realization of the Hofstadter Hamiltonian with ultracold atoms in optical lattices. *Physical Review Letters* **111**, 185301 (2013).
- [10] Jotzu, G. *et al.* Experimental realization of the topological Haldane model with ultracold fermions. *Nature* **515**, 237–240 (2014).
- [11] Goldman, N. & Dalibard, J. Periodically driven quantum systems: Effective Hamiltonians and engineered gauge fields. *Physical Review X* **4**, 031027 (2014).
- [12] Goldman, N., Budich, J. C. & Zoller, P. Topological quantum matter with ultracold gases in optical lattices. *Nature Physics* **12**, 639–645 (2016).
- [13] Zhu, Z., Gächter, M., Walter, A.-S., Viebahn, K. & Esslinger, T. Reversal of quantized Hall drifts at noninteracting and interacting topological boundaries. *Science* **384**, 317–320 (2024).
- [14] Sato, S. A. *et al.* Microscopic theory for the light-induced anomalous Hall effect in graphene. *Physical Review B* **99**, 214302 (2019).
- [15] Merboldt, M. *et al.* Observation of Floquet states in graphene. arXiv:2404.12791 (2024).
- [16] Choi, D. *et al.* Direct observation of Floquet-Bloch states in monolayer graphene. arXiv:2404.14392 (2024).
- [17] Wang, Y. H., Steinberg, H., Jarillo-Herrero, P. & Gedik, N. Observation of Floquet-Bloch states on the surface of a topological insulator. *Science* **342**, 453–457 (2013).
- [18] Zhou, S. *et al.* Pseudospin-selective Floquet band engineering in black phosphorus. *Nature* **614**, 75–80 (2023).
- [19] Schultze, M. *et al.* Controlling dielectrics with the electric field of light. *Nature* **493**, 75–78 (2013).
- [20] Ghimire, S. *et al.* Strong-field and attosecond physics in solids. *Journal of Physics B: Atomic, Molecular and Optical Physics* **47**, 204030 (2014).
- [21] Higuchi, T., Heide, C., Ullmann, K., Weber, H. B. & Hommelhoff, P. Light-field-driven currents in graphene. *Nature* **550**, 224–228 (2017).
- [22] Uzan-Narovlansky, A. J. *et al.* Observation of interband Berry phase in laser-driven crystals. *Nature* **626**, 66–71 (2024).
- [23] Reimann, J. *et al.* Subcycle observation of lightwave-driven Dirac currents in a topological surface band. *Nature* **562**, 396–400 (2018).
- [24] Bauer, D. & Hansen, K. K. High-harmonic generation in solids with and without topological edge states. *Physical Review Letters* **120**, 177401 (2018).
- [25] Soifer, H. *et al.* Band-resolved imaging of photocurrent in a topological insulator. *Physical Review Letters* **122**, 167401 (2019).
- [26] Schmid, C. P. *et al.* Tunable non-integer high-harmonic generation in a topological insulator. *Nature* **593**, 385–390 (2021).
- [27] Heide, C. *et al.* Probing topological phase transitions using high-harmonic generation. *Nature Photonics* **16**, 620–624 (2022).
- [28] Ito, S. *et al.* Build-up and dephasing of Floquet–Bloch bands on subcycle timescales. *Nature* **616**, 696–701 (2023).
- [29] Mitra, S. *et al.* Light-wave-controlled Haldane model in monolayer hexagonal boron nitride. *Nature* **628**, 752–757 (2024).
- [30] Tyulnev, I. *et al.* Valleytronics in bulk MoS₂ with a topologic optical field. *Nature* **628**, 746–751 (2024).
- [31] Eckardt, A. & Anisimovas, E. High-frequency approximation for periodically driven quantum systems from a Floquet-space perspective. *New Journal of Physics* **17**, 093039 (2015).
- [32] Lucchini, M. *et al.* Controlling Floquet states on ultrashort time scales. *Nature Communications* **13**, 7103 (2022).
- [33] Wang, Y., Walter, A.-S., Jotzu, G. & Viebahn, K. Topological Floquet engineering using two frequencies in two dimensions. *Physical Review A* **107**, 043309 (2023).
- [34] Bukov, M. & Polkovnikov, A. Stroboscopic versus non-stroboscopic dynamics in the Floquet realization of the Harper–Hofstadter Hamiltonian. *Physical Review A* **90**, 043613 (2014).

- [35] Neufeld, O., Hübener, H., Giovannini, U. D. & Rubio, A. Tracking electron motion within and outside of Floquet bands from attosecond pulse trains in time-resolved ARPES. *Journal of Physics: Condensed Matter* **36**, 225401 (2024).
- [36] Brida, D., Manzoni, C. & Cerullo, G. Phase-locked pulses for two-dimensional spectroscopy by a birefringent delay line. *Optics Letters* **37**, 3027 (2012).
- [37] Wang, Y. & Gedik, N. Circular dichroism in angle-resolved photoemission spectroscopy of topological insulators. *Physica Status Solidi (RRL) - Rapid Research Letters* **7**, 64–71 (2013).
- [38] Mak, K. F., McGill, K. L., Park, J. & McEuen, P. L. The valley Hall effect in MoS₂ transistors. *Science* **344**, 1489–1492 (2014).
- [39] Neufeld, O., Podolsky, D. & Cohen, O. Floquet group theory and its application to selection rules in harmonic generation. *Nature Communications* **10**, 405 (2019).
- [40] Mrudul, M. S., Jiménez-Galán, Á., Ivanov, M. & Dixit, G. Light-induced valleytronics in pristine graphene. *Optica* **8**, 422–427 (2021).
- [41] Jiménez-Galán, Á., Silva, R. E. F., Smirnova, O. & Ivanov, M. Sub-cycle valleytronics: control of valley polarization using few-cycle linearly polarized pulses. *Optica* **8**, 277–280 (2021).
- [42] Langer, F. *et al.* Few-cycle lightwave-driven currents in a semiconductor at high repetition rate. *Optica* **7**, 276–279 (2020).
- [43] Heide, C., Boolakee, T., Eckstein, T. & Hommelhoff, P. Optical current generation in graphene: CEP control vs. $\omega + 2\omega$ control. *Nanophotonics* **10**, 3701–3707 (2021).
- [44] Hanus, V. *et al.* Light-field-driven current control in solids with pJ-level laser pulses at 80 MHz repetition rate. *Optica* **8**, 570–576 (2021).
- [45] Boolakee, T. *et al.* Light-field control of real and virtual charge carriers. *Nature* **605**, 251–255 (2022).
- [46] Atanasov, R., Haché, A., Hughes, J. L. P., van Driel, H. M. & Sipe, J. E. Coherent control of photocurrent generation in bulk semiconductors. *Physical Review Letters* **76**, 1703–1706 (1996).
- [47] Shapiro, M. & Brumer, P. *Quantum Control of Molecular Processes* (Wiley, 2011).
- [48] Neufeld, O., Tancogne-Dejean, N., Giovannini, U. D., Hübener, H. & Rubio, A. Light-driven extremely nonlinear bulk photogalvanic currents. *Physical Review Letters* **127**, 126601 (2021).
- [49] Weitz, T., Heide, C. & Hommelhoff, P. Strong-field Bloch electron interferometry for band-structure retrieval. *Physical Review Letters* **132**, 206901 (2024).
- [50] Mrudul, M. S. & Dixit, G. Controlling valley-polarisation in graphene via tailored light pulses. *Journal of Physics B: Atomic, Molecular and Optical Physics* **54**, 224001 (2021).

METHODS

Experimental details

We use laser pulses at a fundamental photon energy $\hbar\omega = 0.8\text{ eV}$ (1550 nm central wavelength) with a pulse duration of 170 fs (intensity full width at half maximum,

FWHM) from an amplified 80 MHz erbium-doped fiber oscillator. After frequency doubling in a 1 mm thin type-I phase-matched bismuth borate crystal (BiBO), fundamental and second harmonic (photon energy $2\hbar\omega = 1.6\text{ eV}$, 775 nm central wavelength, 110 fs FWHM) pulse pairs co-propagate with orthogonal linear polarization (Fig. 3b, red and blue envelopes).

A collinear two-color interferometer based on birefringent calcite elements is used to control their relative phase $\varphi_{\omega-2\omega}$ (Fig. 3b) [36]. The first $d_a = 3\text{ mm}$ thin calcite plate is oriented with its ordinary (o) axis parallel to the 2ω polarization and its extraordinary (e) axis parallel to ω ; for the wedged calcite elements, the axes are rotated by 90° to invert the situation. As the two colors experience different refractive indices along the respective axes ($n_\omega^e = 1.47$, $n_\omega^o = 1.64$, $n_{2\omega}^e = 1.48$, $n_{2\omega}^o = 1.65$) this configuration allows us to provide the ω pulses with a head-start after the first calcite plate, which are subsequently caught up by the 2ω pulses in the calcite wedge pair [51]. By finely tuning the inserted thickness d_b of the wedges, the relative phase is controlled as

$$\varphi_{\omega-2\omega} = \frac{2\omega}{c} (d_a \Delta n_{\omega-2\omega}^{oe} + d_b \Delta n_{\omega-2\omega}^{eo}), \quad (1)$$

with $\Delta n_{\omega-2\omega}^{kl} = n_\omega^k - n_{2\omega}^l$. Temporal overlap is determined by maximizing the $\omega + 2\omega$ sum frequency signal obtained from a type-II phase-matched beta barium borate (BBO) crystal in a subsequent reference path. The collinear interferometer design enables a particularly high passive phase stability exhibiting 14.6 mrad integrated jitter in the angular stability of the bigrammatic Lissajous figures over 1 h (see Extended Data Fig. 1). Pulse dispersion upon wedge insertion is negligible as we sample less than four periods of $\varphi_{\omega-2\omega}$ with rather narrow-band spectra at both colors.

For individual control over the ellipticity and rotation of the polarization ellipse of both colors, the delayed pulses are subsequently sent through a sequence of (i) a dichroic half-waveplate acting on 2ω only, (ii) a superachromatic quarter-waveplate acting on both colors, and (iii) a dichroic half-waveplate, which counteracts the ellipsoidal tilt of the 2ω polarization introduced by waveplate (ii) upon rotation of waveplate (i). As waveplate (i) is rotated (Fig. 4), the ellipticity of the 2ω polarization is changed from +1 (waveplate angle 45°) to 0 (22.5°) and -1 (0°), and then back to 0 (22.5°) and +1 (-45°), while the ω polarization is kept constant at circular (ellipticity +1). This sequentially generates the COR, TD and CNR waveforms, and further the TD and COR waveforms with a phase slip of $\Delta\varphi_{\omega-2\omega} = \pi$. We carefully calibrated the waveplates' retardation to a wire-grid polarizer and ensured their dichroic performance with long- and shortpass filters in addition. The resulting bichromatic waveforms are tightly focused onto a sample using a 15 mm off-axis parabolic mirror (Fig. 3b). We measure $1/e^2$ intensity radii of the foci of $2.9\ \mu\text{m}$ (ω) and $1.9\ \mu\text{m}$ (2ω) in color-filtered in-situ knife-edge measurements.

We use a $2 \times 10 \mu\text{m}^2$ strip of epitaxially grown monolayer graphene on silicon carbide as a sample. Its short sides are connected to 30 nm gold electrodes with a 5 nm titanium adhesion layer. Details on the fabrication and characterization are provided in [45]. Gold bond wires connect the electrodes with a chip carrier for photocurrent measurements. All measurements are performed under high vacuum conditions (1×10^{-8} hPa) at room temperature.

For photocurrent detection, we focus the pulse train to the center of the structure such that only the graphene is illuminated. To isolate waveform-dependent currents from photo-thermoelectric currents and other static background, we modulate $\varphi_{\omega-2\omega}$ from pulse to pulse at $f_{\text{mod}} = 117$ Hz with a piezoelectric actuator mounted to one of the calcite wedges. We amplify the resulting current via transimpedance amplification and record it via dual-phase lock-in detection referenced to f_{mod} . Each data point shown in Fig. 4 is recorded with a 300-ms time constant and averaged over 25 data samples. The amplitude of the piezo stroke is calibrated via an external laser diode Michelson interferometer with one end mirror attached to the modulated calcite wedge. When the resulting modulation depth of $\varphi_{\omega-2\omega}$ reaches π , the signal amplitude detected by the lock-in amplifier is maximized. The measured lock-in phase, θ (Fig. 2b), is equivalent to the absolute phase $\varphi_{\omega-2\omega}$ as we determined the temporal overlap of both colors.

Ab-initio TDDFT simulations

We describe here details of the *ab-initio* calculations employed throughout the paper. All calculations are based on TDDFT simulations performed with the open access code Octopus [52]. We solved the time dependent Kohn-Sham (KS) equations of motion, given in the length gauge and atomic units by:

$$i\partial_t\psi_{n,\mathbf{k}}(\mathbf{r},t) = \left(\frac{1}{2}(-i\nabla + \mathbf{A}(t)/c)^2 + v_{\text{KS}}(\mathbf{r},t)\right)\psi_{n,\mathbf{k}}(\mathbf{r},t), \quad (2)$$

where $\psi_{n,\mathbf{k}}(\mathbf{r},t)$ is the KS-Bloch (KSB) state at band index n and k -point \mathbf{k} , and v_{KS} is the KS potential that comprises the classical Hartree interaction term, the interactions of electrons with nuclei and deeper electronic states (which were described by norm-conserving pseudopotentials [53]), and the exchange-correlation (XC) term, where we employed the adiabatic local density approximation (aLDA). We have assumed partial periodic boundary conditions in the graphene monolayer plane (xy), while the z -axis was treated with finite boundary conditions and a complex absorber of width 12 Bohr during propagation (similar to ref. [48]). In eq. 2, $\mathbf{A}(t)$ is the applied vector potential after assuming the dipole approximation, which was taken to have the following form:

$$\mathbf{A}(t) = f(t)cE_0\left(\frac{1}{\omega\sqrt{2}}(\cos(\omega t + \varphi_{\omega-2\omega})\hat{\mathbf{x}} + \sin(\omega t + \varphi_{\omega-2\omega})\hat{\mathbf{y}}) + \frac{1}{2\omega\sqrt{1+\epsilon^2}}(\epsilon\cos(2\omega t)\hat{\mathbf{x}} + \sin(2\omega t)\hat{\mathbf{y}})\right) \quad (3)$$

with c the speed of light, E_0 the electric field amplitude (taken at experimental values), $\varphi_{\omega-2\omega}$ the two-color phase, ϵ the ellipticity of the 2ω field, ω the carrier frequency (taken at the experimental value), and $f(t)$ a temporal envelope (called a ‘super-sine’) taken as [54]:

$$f(t) = \sin\left(\pi\frac{t}{T_p}\right)\left(\frac{|\pi(\frac{t}{T_p} - \frac{1}{2})|}{\sigma}\right), \quad (4)$$

where $\sigma = 0.75$, T_p is the duration of the laser pulse which was taken to be $T_p = 8T$, and $T = 5.17$ fs is a single cycle of the fundamental carrier frequency. This leads to an applied electric field of duration 20.6 fs (FWHM). In eq. 3 by varying the relative phase and ellipticity we obtain the waveforms plotted in the main text.

From the propagation of the KSB states we obtained the current expectation value:

$$\mathbf{J}(t) = \sum_{n,\mathbf{k}} w_k \int [\psi_{n,\mathbf{k}}^\dagger(\mathbf{r},t)\left(\frac{1}{2}(-i\nabla + \mathbf{A}(t)/c) - i[V_{\text{ion}},\mathbf{r}]\right)\psi_{n,\mathbf{k}}(\mathbf{r},t)]d\mathbf{r} + c.c., \quad (5)$$

where V_{ion} is the pseudopotential non-local part of v_{KS} , w_k is the k -point weight, and the sum is performed over occupied states. From $\mathbf{J}(t)$ we calculated the actual measured current by averaging $\mathbf{J}(t)$ over a single cycle of the fundamental frequency after the driving laser pulse has ended (at $t = t_f$): $\mathbf{j} = \int_{t_f}^{t_f+T} \mathbf{J}(t)dt$. We calculated the

projection plots in Fig. 5 by projecting the time dependent KSB states after the laser pulse has ended onto the ground states:

$$g_n(\mathbf{k}) = \sum_m \left| \int \psi_{n,\mathbf{k}}^\dagger(\mathbf{r},t)\psi_{m,\mathbf{k}}(\mathbf{r},t)d\mathbf{r} \right|^2, \quad (6)$$

where the sum runs over occupied states. From $g_n(\mathbf{k})$ we obtained band-resolved occupations, or summed over all conduction/valence bands as presented in Fig. 5. The final occupation plot was also interpolated on a denser k -grid and filtered.

The *ab-initio* calculated phase in Fig. 2b was obtained from the injection current's direction in the xy plane. The valley current in Fig. 2d was calculated by integrating separately for $k_x > 0$ and $k_x < 0$ regions in k -space in eq. 6 for $\mathbf{J}(t)$, and using those quantities to define the normalized contribution of each half of the BZ:

$$J_V = \frac{|\mathbf{j}_K| - |\mathbf{j}_{K'}|}{|\mathbf{j}_K| + |\mathbf{j}_{K'}|}, \quad (7)$$

with $|\mathbf{j}_{K/K'}|$ being the injection current contributed from each region in the BZ.

We performed further auxiliary calculations where the time dependent KS potential was frozen to its ground state form at $t = 0$, i.e. $v_{KS}(\mathbf{r}, t) = v_{KS}(\mathbf{r}, t = 0)$. This yields the independent particle approximation (IPA), where the different KSB states are decoupled from one another in the equations of motion and electron-electron interactions do not evolve dynamically. Figure 2 compares the calculated current from the full TDDFT or IPA simulations for laser parameters similar to the experiment, but taken at an even higher laser power to try and induce larger correlations. The calculated current in both cases agrees remarkably well, indicating that electronic interactions do not play any role in the main mechanisms observed and discussed in the main text.

We further computed the relative occupations of the different valence and conduction bands after the laser pulse ends by integrating $g_n(\mathbf{k})$ from eq. 6 over k -space. From this analysis we find that in typical experimental conditions, over 99.999% of the excitations occur in the first valence and first conduction bands. This result, together with the absence of dynamical interactions shown in Extended Data Fig. 2, validates the model two-band tight-binding Hamiltonian employed in the analytic approach [49].

Lightwave-driven photocurrents in graphene: all cases

The co-rotating circularly-polarized (COR) waveform exhibits a strongly left-right asymmetric Lissajous figure for $\varphi_{\omega-2\omega} = 0$ (Fig. 3a), resulting in a left-right asymmetric intraband trajectory: Electrons initially residing on opposite sides of the Dirac points experience different interband excitation probabilities because they are driven close to the Dirac point (where they are likely lifted to the conduction band), or away from it. As a result, an intra-valley momentum imbalance may be expected (Fig. 3d, red vs. blue shading), generating equal ballistic currents from both valleys [48, 55].

In a third case, we realize valley-selective current generation by an admixture of a linearly polarized second

harmonic with a circularly-polarized fundamental field, the superposition of the COR and CNR cases. The resulting teardrop (TD)-shaped waveform (Fig. 3c) combines the capabilities of intra- and inter-valley symmetry breaking provided by the COR and CNR waveform. Strikingly, the TD waveform can generate a current with selectivity between the K and K' valley [56–58] (Fig. 3f), resulting in a *valley current*, i.e., a current from one valley only.

Despite the valley selectivity for the TD shape, the total current density is only decreased experimentally by 33% of its global maximum obtained for the COR waveform (Fig. 4b, purple circles), suggesting this excitation as a viable approach to valley polarized current generation. Moreover, we have full control over the valley to be addressed by changing $\varphi_{\omega-2\omega}$ by π and the direction of valley current flow by inverting the helicity of the fundamental.

Comprehensive symmetry analysis

To investigate the origin of the photocurrents, we model the time-dependent dynamics with both analytic and *ab-initio* methods. In Extended Data Figure 3 we present the CNR analysis discussed around Fig. 5 again, highlighting the local symmetries, for clarity. Extended Data Figures 3a–l show the residual conduction band distributions for the COR and CNR waveforms obtained from TDDFT. Analyzing all six K and K' points allows us to look at the dynamical selection rules for the respective waveforms globally, while the zoom-ins (Extended Data Figs. 3e–h) highlight the intra-valley symmetries.

We analyze the dynamical selection rules by the residual conduction band populations for two orthogonal phases of both the COR and CNR waveforms. After excitation with the COR waveform (Extended Data Figs. 3a–b) we can see one mirror axis present in each of the graphene band structures corresponding to the waveform symmetry. For $\varphi_{\omega-2\omega} = \pi/2$ (Extended Data Fig. 3a), we observe a left/right symmetry in the conduction band population, resulting in no current generation, with a dominate symmetry axis through M– Γ –M', addressing the K and K' points equivalently, rendering ρ^c K and K' symmetric. The zoom in (Extended Data Fig. 3e) highlights the crescent features showing this vertical mirror axis between the K and K' points. When $\varphi_{\omega-2\omega} = 0$ (Extended Data Figs. 3b,f), our waveform's principle symmetry axis changes to the K– Γ –K' axis. This disconnects the K and K' points and allows intra-valley momentum imbalances and a net current.

For the excitation with a CNR waveform (Extended Data Figs. 3c–d), similar arguments can be made, now with the waveforms exhibiting two additional minor mirror axes (dashed orange lines) corresponding to the three-fold rotational symmetry of the waveform. Importantly, the time reversal symmetry (purple color bar) is coupled to the primary mirror axis (green). Critically, shown in

the $\varphi_{\omega-2\omega} = \pi/2$ waveform, the symmetry axis connects K and K' (a M- Γ -M' axis), resulting in the inability to generate a valley polarization. With $\varphi_{\omega-2\omega} = 0$, the waveform's symmetry axis (K- Γ -K') now disconnects the K and K' points, resulting in possible valley polarization. The zoom-ins of the CNR population (Extended Data Fig. 3g-h) reveal the local symmetries (dashed orange lines) within the K and K' valleys.

To understand the emergence of these characteristic patterns (seen in Extended Data Figs. 3f,h) and the underlying valley control on a sub-cycle time scale, it is insightful to discuss a picture of time-dependent inter- and intraband electron dynamics in the undressed band structure. We highlight these dynamics for three exemplary electrons with initial momenta equidistant to the respective K and K' point (Extended Data Figs. 3f,h, colored circles). Extended Data Figs. 3j,l show the respective sub-cycle evolution of the interband dipole coupling $V^{cv}(t)$ induced by the COR and CNR waveform, respectively (both at $\varphi_{\omega-2\omega} = 0$). The stark inter-valley differences in $|V^{cv}|$ occurring during the center optical cycle (Extended Data Figs. 3i,k; shaded areas) become clear with a fundamental field strength of 1 V nm^{-1} applied here for visibility.

The COR waveform drives the right marked electron in the K' valley (Extended Data Fig. 3f) close to the Dirac point, resulting in a large excitation probability (Extended Data Fig. 3j), whereas it is suppressed for the other two marked electrons, which are driven away from the Dirac point. Hence all three exemplary electrons are shown to assist in the generation of intra-valley momentum asymmetry, observed in the crescent shaped distribution of Extended Data Fig. 3f and measured as a large current (Fig. 4b). The three marked electrons in the K valley contribute likewise.

In contrast, the CNR waveform drives all three exemplary electrons in the K' valley (Extended Data Fig. 3h) equally close to the Dirac point. At the K point, the same three electrons come close to the Dirac point only for a highly confined duration at the trefoil peaks, lowering their excitation probability. In the dipole coupling (Extended Data Fig. 3l) this is reflected in a larger amplitude of $|V^{cv}|$ for each electron around K' compared to K. Importantly, these valley-specific differences in interband coupling result in a valley-polarized conduction band population. In addition, since the relative amplitudes of the marked points are not exchanged between K and K' (as is the case for the COR waveform, Extended Data Fig. 3l), there is no intra-valley momentum asymmetry. This allows us to identify the drastic reduction of the measured current (Fig. 4b) as an experimental generation of valley-polarized graphene.

DATA AVAILABILITY

Source data are provided with this paper. All other data that support the plots within this Article and other

findings of this study are available from the corresponding author(s) upon reasonable request.

ACKNOWLEDGEMENTS

We thank Sebastian Lotter and Heiko B. Weber for providing the sample, and Anna Galler for helpful discussions. P.H. thanks Gregor Jotzu for various discussions. This work has been funded by the Deutsche Forschungsgemeinschaft (SFB 953 'Synthetic Carbon Allotropes', 182849149), the PETACom project financed by Future and Emerging Technologies Open H2020 program, ERC Grant AccelOnChip (884217), and the Gordon and Betty Moore Foundation (GBMF11473). C.H. acknowledges support from the Alexander von Humboldt Research Fellowship and US Department of Energy, Office of Science, Basic Energy Sciences, Chemical Sciences, Geosciences, and Biosciences Division through the AMOS program.

AUTHOR INFORMATION

Authors and Affiliations

Physics Department, Friedrich-Alexander-Universität Erlangen-Nürnberg (FAU), Erlangen, Germany

Tobias Weitz, Daniel M. B. Lesko, Simon Wittigshlager, Weizhe Li, Christian Heide, & Peter Hommelhoff

Stanford PULSE Institute, SLAC National Accelerator Laboratory, Menlo Park, CA, USA

Christian Heide

Max Planck Institute for the Structure and Dynamics of Matter, Hamburg, Germany

Ofer Neufeld

Contributions

P.H. and T.W. conceived the study. T.W. and S.W. performed the experiment with input from C.H.. T.W. and D.M.B.L. analyzed the results. O.N., D.M.B.L., T.W. and W.L. performed the simulations. D.M.B.L., T.W., O.N. and P.H. wrote the manuscript with input from all authors.

Corresponding authors

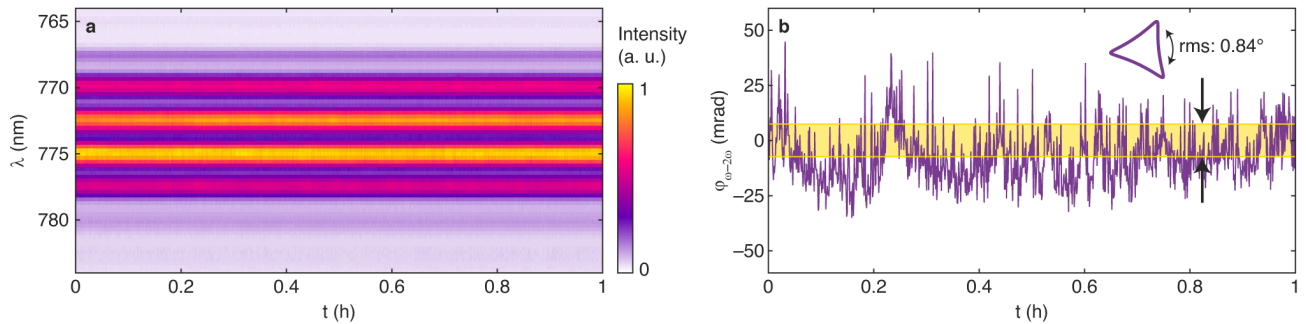
Correspondence to Daniel Lesko, Ofer Neufeld and Peter Hommelhoff.

ETHICS DECLARATIONS

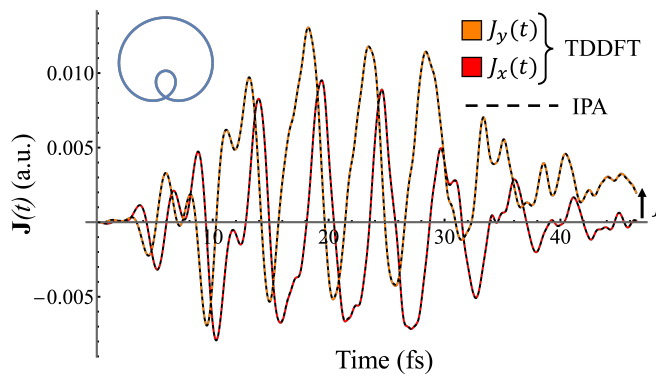
Competing interests

A subset of the authors have filed a patent titled “Method and apparatus for generating valley current in a solid material” (EP24175546.1).

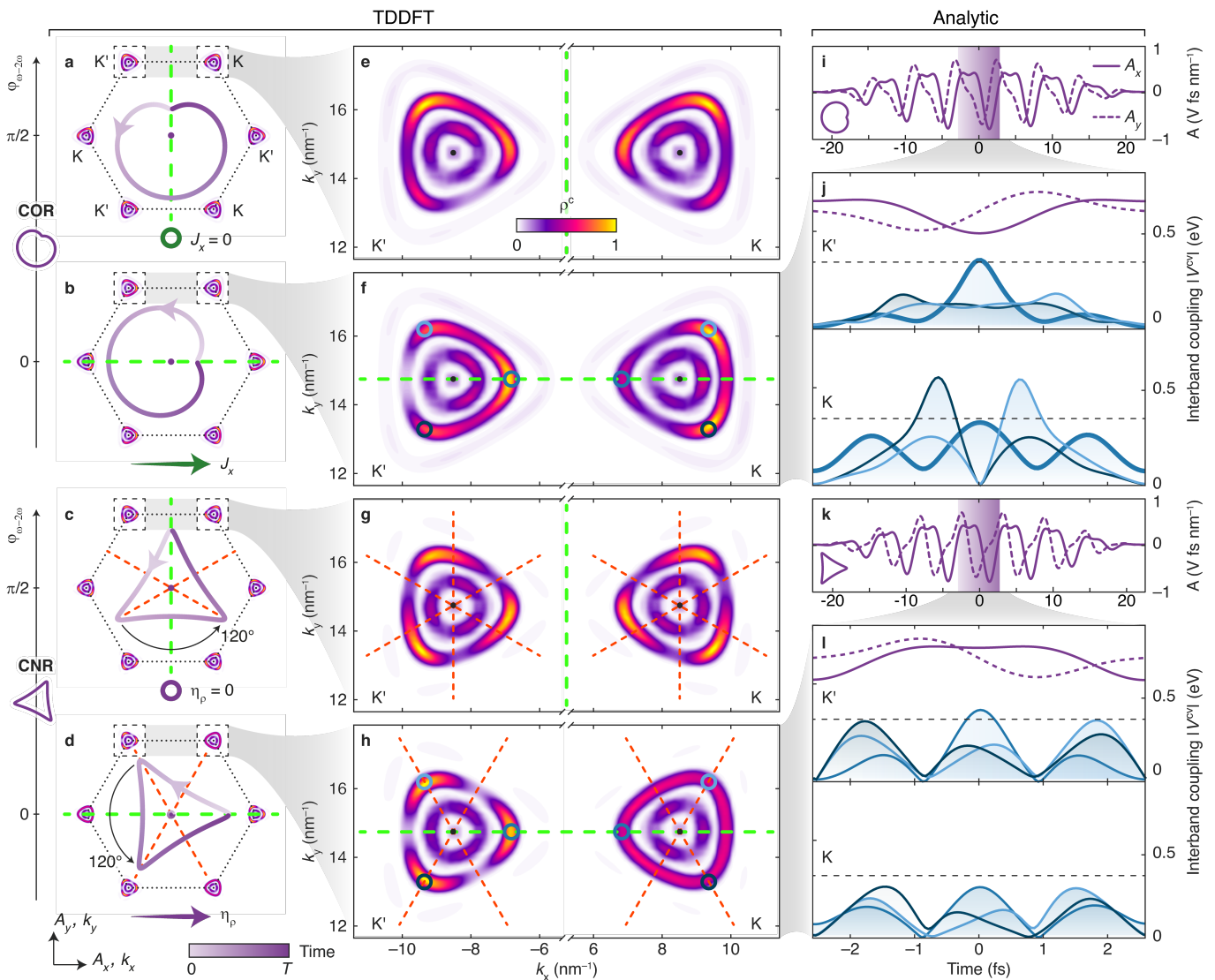
-
- [51] Ghosh, G. Dispersion-equation coefficients for the refractive index and birefringence of calcite and quartz crystals. *Optics Communications* **163**, 95–102 (1999).
- [52] Tancogne-Dejean, N. *et al.* Octopus, a computational framework for exploring light-driven phenomena and quantum dynamics in extended and finite systems. *The Journal of Chemical Physics* **152**, 124119 (2020).
- [53] Hartwigsen, C., Goedecker, S. & Hutter, J. Relativistic separable dual-space Gaussian pseudopotentials from H to Rn. *Physical Review B* **58**, 3641–3662 (1998).
- [54] Neufeld, O. & Cohen, O. Background-free measurement of ring currents by symmetry-breaking high-harmonic spectroscopy. *Physical Review Letters* **123**, 103202 (2019).
- [55] Heide, C., Higuchi, T., Weber, H. B. & Hommelhoff, P. Coherent electron trajectory control in graphene. *Physical Review Letters* **121**, 207401 (2018).
- [56] Jiang, Y., Low, T., Chang, K., Katsnelson, M. I. & Guinea, F. Generation of pure bulk valley current in graphene. *Physical Review Letters* **110**, 046601 (2013).
- [57] Sharma, S., Gill, D. & Shallcross, S. Giant and controllable valley currents in graphene by double pumped THz light. *Nano Letters* **23**, 10305–10310 (2023).
- [58] Sharma, S., Dewhurst, J. K. & Shallcross, S. Light-shaping of valley states. *Nano Letters* **23**, 11533–11539 (2023).



Extended Data FIG. 1. **Phase stability of the collinear interferometer.** **a**, Interference fringes at 2ω measured every 35 ms for 1 h with a spectrometer integration time of 10 ms. **b**, Reconstructed jitter of $\varphi_{\omega-2\omega}$ obtained from a cosine square fit, yielding a root mean square of 14.6 mrad (0.84°) for the angular stability of the bichromatic Lissajous figures (yellow shading).



Extended Data FIG. 2. **Comparison of calculated current expectation value, $\mathbf{J}(t)$ from eq. 6, with a full TDDFT calculation, or within the IPA with frozen electronic interactions.** The system's response is almost identical in both cases, indicating the interactions are negligible. Calculated for co-circular case at a high laser power of 10^{11} W/cm^2 with 1550nm driving.



Extended Data FIG. 3. **Sub-cycle dynamical symmetry selection rules.** **a–d**, Temporal shape and symmetries of the vector potential Lissajous figures (purple lines) and the resulting symmetries of residual momentum distributions ρ^c imprinted to the first Brillouin zone (dotted hexagons) for the COR (**a**, **b**) and CNR waveform (**c**, **d**) for $\varphi_{\omega-2\omega} = \pi/2$ and 0 respectively. The momentum distributions are computed with TDDFT (see Methods for details). Green (orange) dashed lines indicate global (valley-specific) symmetry axes, determined by both waveform and time periodicity (see purple color bar). **e–h**, Close-ups of ρ^c around K and K' as indicated in **b**, **d**. For all cases, an eight-cycle pulse (super-sine envelope, see vector potential in **i** and **k**) is applied with 1550 nm fundamental wavelength with a peak field strength $E_0 = 0.27 \text{ V nm}^{-1}$ and 75% 2ω field admixture. **i**, **k**, COR (**i**) and CNR (**k**) vector potential waveform for $\varphi_{\omega-2\omega} = 0$. The shaded areas indicate the center optical cycle respectively. **j**, **l**, Temporal profile of the interband dipole coupling $|V^{cv}|$ [49] induced by the waveforms shown in **i** and **k**, respectively. The different shades of blue refer to initial momenta in the K and K' valley as marked with circles in panels **e–h**. The dashed black guide lines compare the $|V^{cv}|$ amplitudes at K and K'.